Research on Response Characteristics of GPR Method for Detecting Phreatic Lines in Embankments

Yan Chen[1, a], Shengxing Zhang[1, b], Lei Tang[1, c]

[1] Nanjing Hydraulic Research Institute, Nanjing, Jiangsu, China.

[a] alickchen021@163.com, [b] sxzhang@nhri.cn, [c] ltang@nhri.cn

Abstract. The excessive elevation of the phreatic lines under continuous high-water levels is the cause of many dangerous situations in embankments. Therefore, accurately understanding the dynamic changes in the infiltration characteristics of embankments is of great significance for judging and evaluating the stability of engineering. This study conducted indoor model experiments and used ground penetrating radar to detect the phreatic lines of soil. By comparing the radar detection results with the measured position of the phreatic lines, it was determined that the phreatic lines appeared as a continuous strong reflection surface with similar shapes in the radargram, and the reflection below the reflection surface became weaker. Through time-domain analysis of the single waveform at different time points, it was found that the amplitude of the reflected wave at the saturation line was larger, and the energy attenuation below the saturation line was faster, resulting in a rapid decrease in amplitude; perform Fourier transform on a single channel signal to obtain a spectrogram, and perform frequency domain analysis on it. The main frequency is around 600MHz, and the second main frequency is around 900MHz. As the saturation line rises, the main frequency gradually shifts towards lower frequencies.

Keywords: GPR; Phreatic line; Time-domain analysis; Frequency-domain analysis.

1. Introduction

Flood disasters have always been a major concern for the Chinese nation, and embankments are the key barrier to resist flood disasters. The total length of Grade 5 and above embankments in China is 328000 kilometers, of which 240000 kilometers have reached the standard, with a compliance rate of 73.0%. Among them, the length of Grade 1 and Grade 2 compliant embankments is 37000 kilometers, with a compliance rate of 83.1% [1]. Most of the active embankments in our country were built between the 1950s and 1970s. Due to various factors such as socio-economic conditions and construction technology during that period, a large number of embankments had internal hidden dangers. During the flood season, embankment dangers continued to occur frequently and suddenly, and rescue tasks were heavy. One of the important reasons was that it was difficult to quickly grasp the stability status of embankments and predict embankment risks during the flood season, leading to minor ailments and the development of hidden dangers into disasters. During the flood season or when high water levels persist, water in front of the embankment seeps into the interior, causing the phreatic lines to rise and causing scattered flooding on the back slope. When the phreatic lines are raised too much, it may develop into dangerous situations such as slope detachment and loopholes. Therefore, accurately grasping the dynamic changes in the infiltration characteristics of embankments is of great significance for judging and evaluating the evolution process of embankment diseases, engineering stability evaluation, and later operation and maintenance [2]. In order to solve the above problems, this study introduces the ground-penetrating radar (GPR) method to quickly obtain physical field parameters related to the behavior of embankments. This method can quickly detect hidden dangers such as water accumulation, leakage, and ant nests inside embankments, and effectively detect soil moisture content to determine the development of phreatic lines. Compared with traditional soil mechanics parameter testing methods, it has advantages such as non-destructive, fast, in-situ detection, continuous detection, and applicability to various geological conditions [3].

In the research of domestic and foreign scholars, GPR has been widely used in engineering hazard detection, glacier thickness detection, and concrete moisture content calculation. Hong

Xiaogang and others used GPR to collect radar signals of asphalt pavement structural cracks and interlayer discontinuous diseases, obtained measured profiles, and combined with deep learning model recognition technology to achieve accurate identification of cracks [4]. Zuo Jing and others used GPR technology to detect the dam body and foundation, qualitatively judge the layering, cracks, hole positions, and development trends of the soil layer, and analyze the development of hidden dangers in the dam [5]. Zhou Liming and others used GPR technology to accurately detect the glacier thickness of the main peak of Gela Dandong, the source of the Tuotuo River. They inferred that the location of d=4.7m underground is the upper limit of frozen soil, which is basically consistent with the measured freezing position d=4.73m in the on-site groundwater monitoring well [6]. Kaplanvural used particle swarm optimization (PSO) to invert the trajectory of GPR to study the volumetric moisture content of concrete blocks. Using the PSO method as the inversion tool, the PSO method was applied to a GPR dataset containing 24 days of data to estimate the relative dielectric permittivity values and calculate the volumetric moisture content of concrete [7]. Xu Zeshan and others found through forward simulation combined with practical engineering applications that for filling and repairing voids with traditional materials that have little difference in electrical properties from the original roadbed materials, GPR can accurately detect the repair effect [8]. Dagenbach and others conducted semi-quantitative analysis based on numerical simulation of radar signals and conducted suction and drainage experiments at ground penetrating radar locations for evaluation. By establishing a fluctuating groundwater level, the ground penetrating radar antenna recorded the relationship between fixed positions and time. By measuring, capillary edges in soil can be identified and tracked. Based on the recorded radar images, the typical dynamics of soil moisture content with transient water levels can be derived [9]. Jafarov and others conducted a series of ground penetrating radar and detection surveys near Barrow, Alaska, using a 500 MHz antenna and metal detector. Approximately 15 kilometers of ground penetrating radar data and 1.5 kilometers of detection data was collected. The GPR data processing flow for estimating the active layer thickness (ALT) and volumetric water content (VWC) using the original GPR data simultaneously includes the corresponding uncertainty of each measurement and estimation parameter. The estimated average value of ALT for GPR inversion is 41 cm, with a standard deviation of 9 cm. The average detection ALT is 40 cm, with a standard deviation of 12 cm. The average VWC value of GPR inversion is 0.65, with a standard deviation of 0.14 [10]. Shamir and others developed a mixed model based on soil texture, porosity, and effective dielectric constant for measuring soil moisture content (SMC) in large-scale underground spaces. By analyzing the propagation time of ground penetrating radar reflection and diffraction waves, the electromagnetic velocity, effective dielectric constant, and spatial SMC under laboratory conditions can be calculated [11]. Leger and others studied the use of ground penetrating radar data obtained during water infiltration to obtain the Mualem-van Genuchten (M-vG) hydraulic parameters of sandy soil. Based on the initial values of the M-vG parameter, SWMS-2D is used to simulate the water distribution with different infiltration time steps, and a complex refractive index model is used to convert it into the distribution of dielectric constant [12].

Although the application range of GPR method is wide, there is relatively little research in the field of response characteristic analysis for detecting phreatic lines in embankments. To explore this issue, indoor experiments will be conducted in this study. By comparing the radar detection results with the actual observation and measurement of the position of the phreatic lines, the manifestation and characteristics of the phreatic lines in the radargram will be preliminarily determined. The characteristics of the phreatic lines in the radar detection results will be further identified through time-domain analysis and frequency-domain analysis. Finally, the relationship between the radar detection results and the soil phreatic lines will be established.

2. Detecting principle

GPR is a technology that uses pulsed electromagnetic waves to detect the spatial position,

structure, and distribution of underground targets. GPR detection typically uses a pair of antennas for operation. Electromagnetic pulse waves with a certain center frequency are emitted from the transmitting antenna into the underground medium. When electromagnetic pulse waves propagate in the underground medium, they will reflect, transmit, and refract when encountering the interface of electromagnetic properties (resistivity, dielectric permittivity values, and magnetic permeability) in the medium. The reflected and refracted electromagnetic waves will return to the surface and be received by the receiving antenna. GPR has three types of echo signals: air direct wave, ground direct wave, and reflected wave. Some of the electromagnetic waves propagate directly through the air to the receiving antenna, as shown in Fig. 1, which is called air direct wave [13]. In addition, the relative resistivity of air is 1. Due to the small attenuation of electromagnetic waves in air, it can be used to represent the intensity of electromagnetic waves during emission [14]. The electromagnetic waves emitted by the transmitting antenna, passing through the soil layer near the ground and received by the receiving antenna are called ground direct waves, and their propagation process in the soil near the ground can be regarded as the distance between two antennas. It is generally believed that the effective depth detectable by ground direct waves is between 0.1 and 0.25m. Reflected waves are signals emitted by transmitting antennas, received by receiving antennas, and the reflected information is extracted and analyzed to obtain information such as velocity and dielectric permittivity values. The signal received by the receiving antenna is processed and converted into a time series signal. This time series at each measuring point constitutes the radar waveform recording track of that measuring point, which contains information such as the amplitude, phase, and two-way travel time of the radar wave received at that measuring point [13].

The soil below the phreatic lines is in a saturated state due to water infiltration, while the soil above the phreatic lines is in an unsaturated or dry state. The dielectric permittivity values of saturated soil increase significantly, and a clear electrical interface is formed between it and other soil [15]. Therefore, this characteristic can be used to determine the position of the phreatic lines on the radargram.

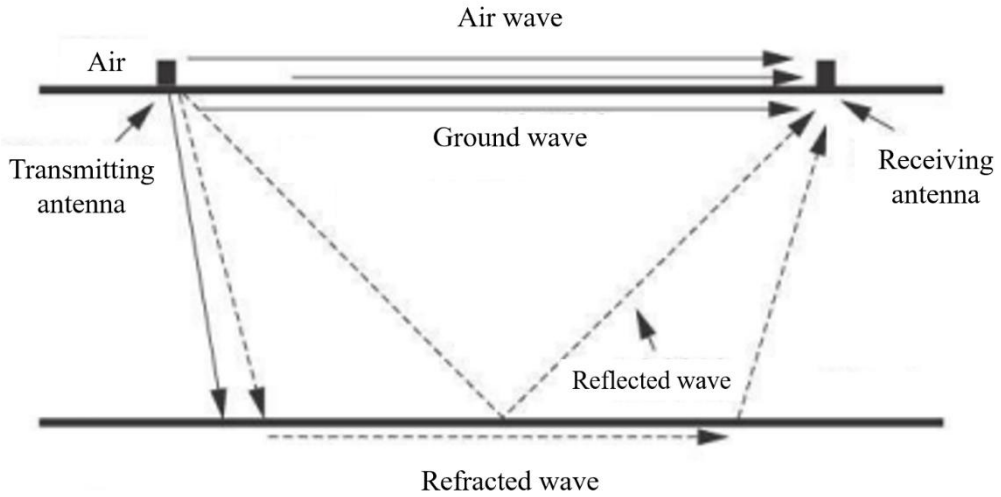

Fig. 1 Schematic diagram of the propagation path of radar waves in a double-layer medium

3. Indoor model experiment

3.1 Experiment model

A model experiment box with dimensions of 1.2m x 0.5m x 0.5m (length x width x height) was used in this experiment, as shown in Fig. 2 (a). The side of the model experiment box is closed and the top surface is open, making it convenient for soil filling and water lifting and lowering tests to be carried out. The model experiment box is made of transparent acrylic board, which facilitates the observation of the state of the experiment model and the phreatic lines. Place a partition 20cm away

from the left panel to separate the entire model experiment box into two areas. The left side is the water storage area, which is used for water storage and simulates different water level conditions by changing the water level height; On the right is the filling area, which is filled with the experimental model soil. On the left side panel, a circular hole with a diameter of 3cm is opened at the bottom of the centerline, and a drainage pipe and water valve are installed on the outer side. A circular hole with a diameter of 2cm is opened on the centerline 20cm, 30cm, and 40cm away from the bottom, and a drainage pipe and water valve are installed on the outer side to control the water level in the storage area. The right panel is identical to the left side panel and is used to drain water from the fill area. A circular hole with a diameter of 3cm is opened at the bottom of the middle of the front side panel, and a drainage pipe and water valve are installed on the outside, which is also used to discharge water from the filling area. Place a geotextile at the opening of the right panel and the front side panel to block the drainage pipe with soil, as shown in Fig. 2 (b) and Fig. 2 (c). Several rectangular and circular holes are drilled on the middle partition to allow water in the storage area to infiltrate the soil in the filling area. A geotextile is placed on the filling side of the partition to facilitate filling, as shown in Fig. 2 (d). Mark several points with a black oily pen at the top of the filling area on the front side panel as distance markers, with a distance of 14cm from the middle partition and panel, and every 15cm between the two points as distance markers.

After sufficient compaction and drying of the soil required for the experiment, it is filled into a model experiment box with a soil height of about 43cm. During the filling process, a layered compaction construction process is adopted to ensure the compactness of the soil filling. Divide the soil into six soil layers from shallow to deep, as shown in Fig. 2 (f). The specific parameters of each soil layer are as follows: (1) The depth of the layer is 0~18cm, and the soil used is silty loam with a dielectric permittivity values of 4.9; (2) The layer depth is 18~30cm, which is a silty loam with a dielectric permittivity values of 6.4; (3) The layer depth is 30~31cm, which is a powdery clay with a dielectric constant of 6.9; (4) The layer depth is 31~33cm, which is sandy soil with a dielectric permittivity values of 5.9; (5) The layer depth is 33~40cm, which is a silty loam with a dielectric permittivity values of 6.5; (6) The depth of the layer is 40~43cm, which is a silty loam with a dielectric permittivity values of 6.6.

(a) Model experiment box

(b) Geotextile at the right panel

(c) Geotextile at the front panel (d) Geotextile at the middle partition

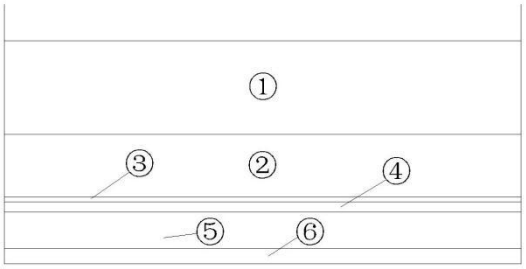

(e) Experiment model (f) Schematic diagram of soil layer

Fig. 2 Indoor Experiment Model

3.2 Experiment equipment

The GPR equipment adopts the LTD-2600 new intelligent GPR system, as shown in Fig. 3. This system consists of a radar host developed based on the Android system, seamless compatibility with the latest high-frequency antenna series, and powerful acquisition and post-processing software, which can be widely used in engineering detection and geological exploration fields. Due to the small size of the model in this experiment, which requires high resolution but low detection depth, a 900MHz shielded antenna is equipped. The antenna is compact and flexible, and has a handle on the top that is easy to grip, making it easy to operate. The specific parameters of radar host and antenna are shown in Table 1 and Table 2.

Table 1. Parameters of 900MHz shielded antenna

Name	Parameter
Device Name	GC900 MHz
Size(cm)	29.5×21.5×16.5
Weight(kg)	1.9
Detection depth (m)	0.05~1.0
Thickness/depth detection error	<6%
Offset(cm)	13
Emission amplitude (V)	60

Table 2. Parameters of LTD-2600 radar host

Name	Parameter
Device Name	LTD-2600
Size(cm)	34×26.8×7
Weight(kg)	3.5
Display method	Pseudo color image, stacked waveform or grayscale image
Scanning rate(Hz)	16/32/64/128/256/512/1024
Trace length	128/256/512/1024/2048/4096/8192
Real time software processing function	Filtering, amplification, inter channel averaging, and background removal processing
Dynamic range(dB)	-7~130
Measurement method	Point measurement, distance triggered measurement, continuous measurement

(a) LTD-2600 Radar host (b) 900MHz antenna

Fig. 3 GPR devices

3.3 Experiment process

Before adding water, use GPR to detect the dry soil. Then, fill the left area of the model experiment box with water and maintain a water level of 10cm. Take photos and record the changes of the phreatic lines in the current soil at regular intervals, as shown in Fig. 4. At the time of 30 minutes and 60 minutes, the GPR was used to detect along the top centerline of the soil twice in both forward and reverse directions. Afterwards, the water level was raised to 20cm and the above experiment process was repeated again. The changes of the phreatic lines are shown in Fig. 5.

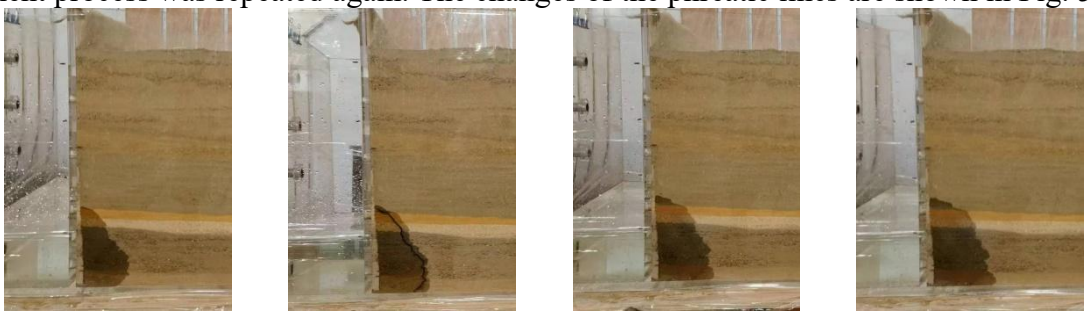

(a)5min (b)10min (c)15min (d)20min

(e)25min (f)30min (g)40min (h)50min

(i)60min (j)70min (k)80min

Fig. 4 The variation of soil phreatic lines at a water depth of 10cm

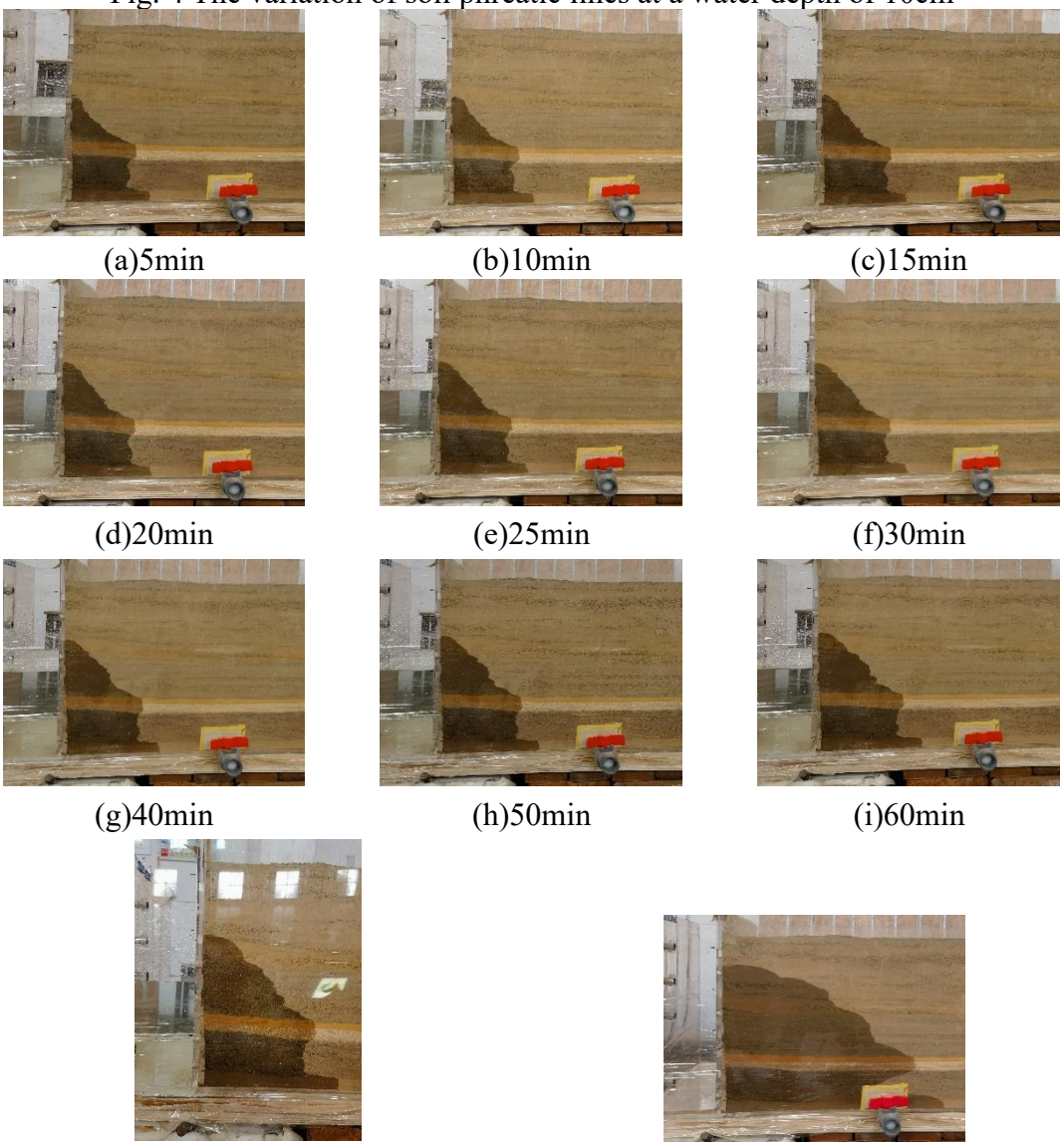

(a)5min (b)10min (c)15min

(d)20min (e)25min (f)30min

(g)40min (h)50min (i)60min

(j)80min (k)16.5h

Fig. 5 The variation of phreatic lines at a water level of 20cm

4. Experiment results and analysis

4.1 Radargram

The radargrams under different water levels are shown in Fig. 6. As shown in Fig. 6 (a), two obvious reflection layers appear at depths of 0.3m and 0.4m. The reflection layers are continuous on the same phase axis and relatively straight, suggesting an interface between the two soil layers. Due to significant changes in the dielectric permittivity values at the interface, the reflection signal characteristics are obvious. After comparing with the actual situation of the experiment model, its position matches the actual situation, indicating that the detection results of this GPR are reliable. In addition, in the radargram shown in Fig. 6 (b), a tilted strong reflection surface is presented at a depth of about 0.3m. Comparing it with the actual observation results in Fig. 4 (f), the positions and depths of the two are basically consistent, and it can be determined that this strong reflection surface is the phreatic lines of the soil. Further comparing the radargram in Fig. 6 with the soil phreatic lines images in Fig. 4 and Fig. 5, it can be observed that the radar waves have significant reflections at the phreatic lines, and as the phreatic lines rises, the height of the reflection area in the

radargram also increases accordingly.

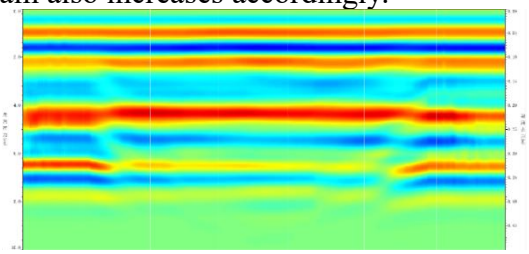

(a)Radargram in dry state

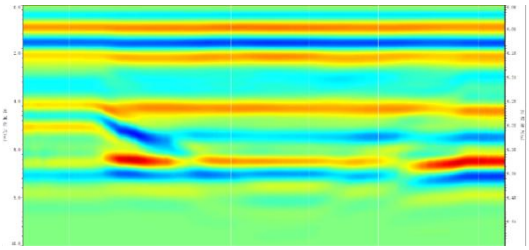

(b)Radargram at a water level of 10cm for 30min

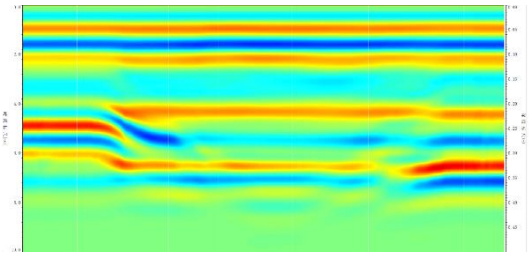

(c) Radargram at a water level of 10cm for 60min

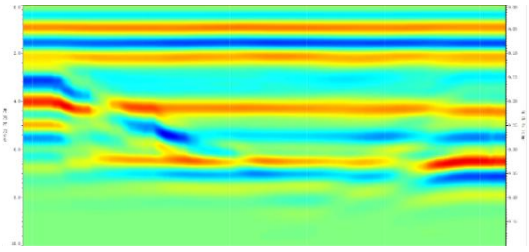

(d) Radargram at a water level of 20cm for 30min

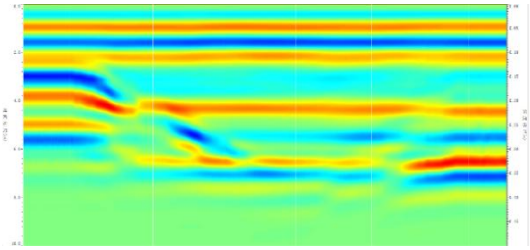

(e) Radargram at a water level of 20cm for 60min

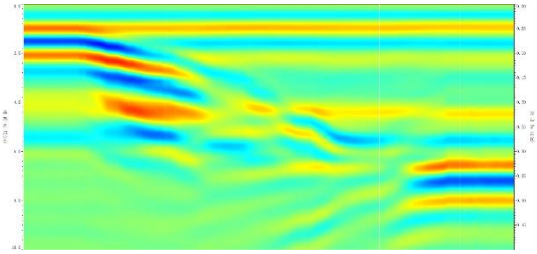

(f) Radargram at a water level of 20cm for 16.5h

Fig. 6 Variation of radargrams

4.2 Instantaneous attribute analysis

The commonly used instantaneous signal parameters mainly include three, namely instantaneous amplitude, instantaneous frequency, and instantaneous phase, also known as the three instantaneous parameters. The three instantaneous parameters are mainly obtained from actual information through Hilbert transformation. Assuming that the original actual information is x(t), the analytical information y(t) obtained through Hilbert transformation is as follows:

$$y(t)=\frac{x(t)}{\pi t}=\frac{1}{\pi}\int_{-\infty}^{+\infty}\frac{x(\tau)}{t-\tau}d\tau \#(1)$$

The instantaneous amplitude A(t), instantaneous phase θ(t) and instantaneous frequency ω(t) obtained by Hilbert transformation of the original information x(t) are as follows:

$$A(t)=\sqrt{x(t)^2+y(t)^2}\#(2)$$

$$\theta(t)=\arctan\frac{y(t)}{x(t)}\#(3)$$

$$\omega(t)=\frac{d\theta(t)}{dt}\#(4)$$

The instantaneous amplitude obtained through Hilbert transform is shown in Fig. 7, the instantaneous phase is shown in Fig. 8, and the instantaneous frequency is shown in Fig. 9.

The instantaneous amplitude reflects the strength of the reflected signal, and the overall shape is similar to the radar detection spectrum. It highlights the strong reflection characteristics of the soil layer interface and soil phreatic lines, and to some extent suppresses some clutter. The color of the soil infiltration area is darker than the surrounding area, which can more clearly distinguish the

shape and boundary of the soil infiltration area.

The instantaneous phase reflects the continuity of adjacent signals, which is independent of the strength of the reflected signal, and the weak amplitude can also be reflected in the graph, with high resolution. In Fig. 8, both the interface of the soil layer and the phreatic lines show clear continuous in-phase axes, while in the area below the phreatic lines, there is a clear discontinuity in the in-phase axis, indicating the presence of anomalies, as shown in Region A in Fig. 8 (b) ~Fig. 8 (f).

The instantaneous frequency reflects the rate of change in phase over time, and significant changes occur at the interface of different media. Therefore, each interface can be easily and efficiently observed from the instantaneous frequency graph. Starting from Fig. 9 (b), the bottom of the initial detection stage is the wetted area, resulting in instantaneous frequency oscillation, which corresponds to the phenomenon in the instantaneous phase image.

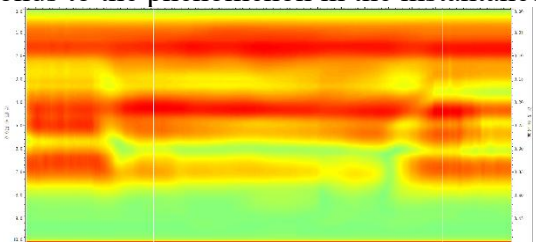

(a)Radargram in dry state

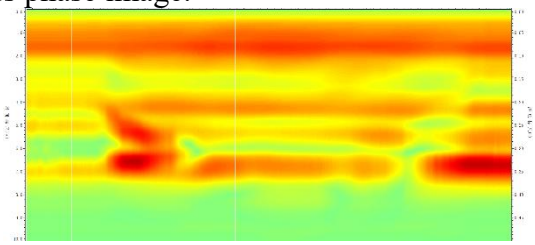

(b)Radargram at a water level of 10cm for 30min

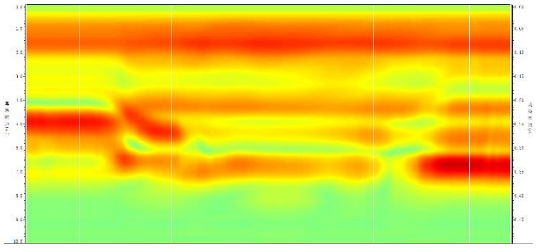

(c) Radargram at a water level of 10cm for 60min

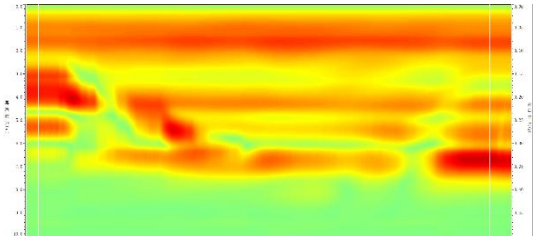

(d) Radargram at a water level of 20cm for 30min

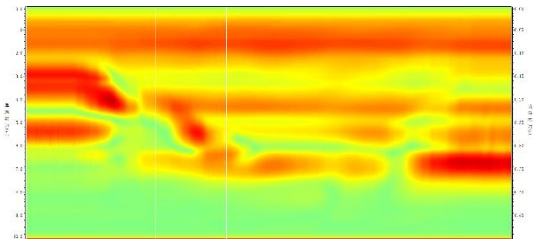

(e) Radargram at a water level of 20cm for 60min

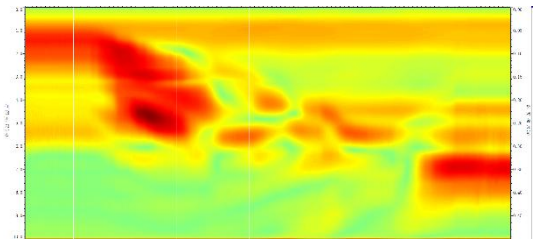

(f) Radargram at a water level of 20cm for 16.5h

Fig. 7 Instantaneous amplitude

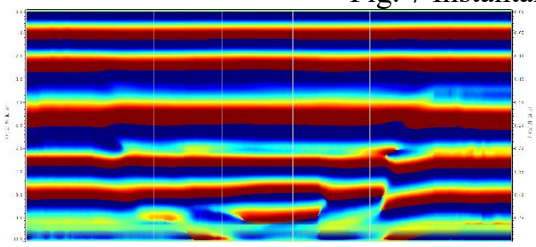

(a)Radargram in dry state

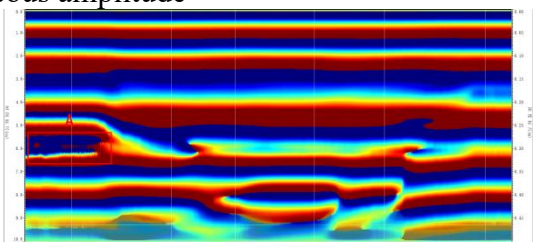

(b)Radargram at a water level of 10cm for 30min

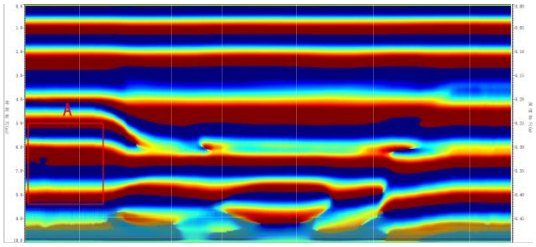

(c) Radargram at a water level of 10cm for 60min

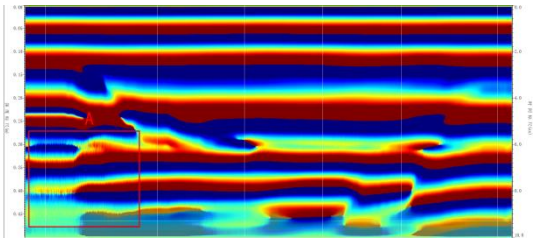

(d) Radargram at a water level of 20cm for 30min

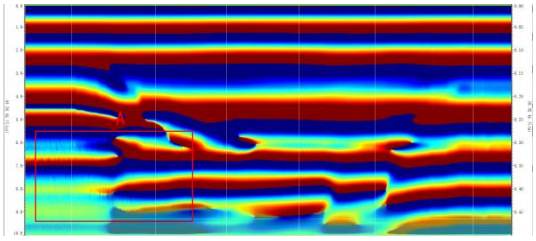

(e) Radargram at a water level of 20cm for 60min

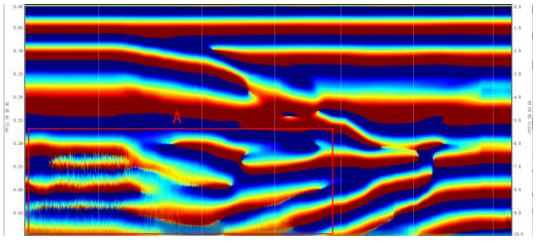

(f) Radargram at a water level of 20cm for 16.5h

Fig. 8 Instantaneous phase

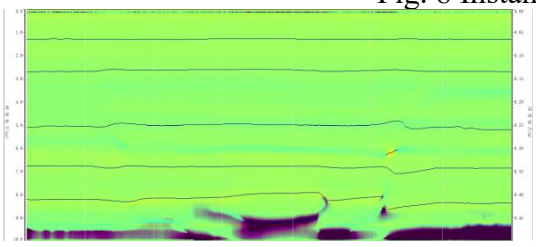

(a)Radargram in dry state

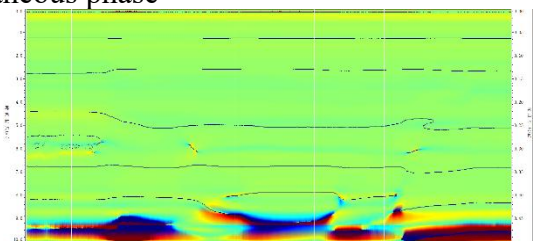

(b)Radargram at a water level of 10cm for 30min

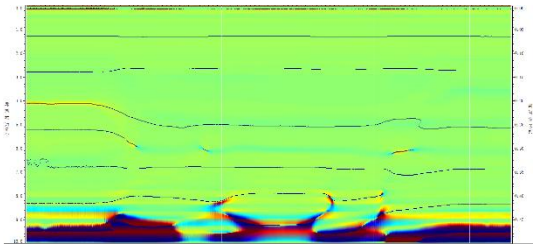

(c) Radargram at a water level of 10cm for 60min

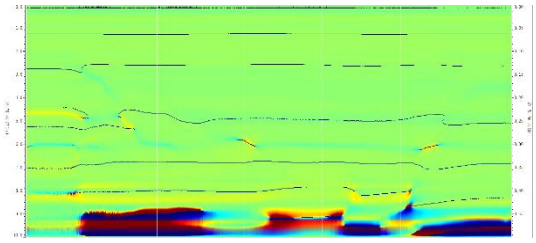

(d) Radargram at a water level of 20cm for 30min

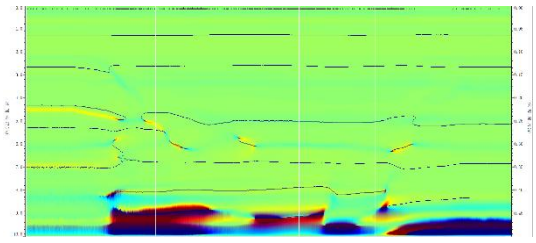

(e) Radargram at a water level of 20cm for 60min

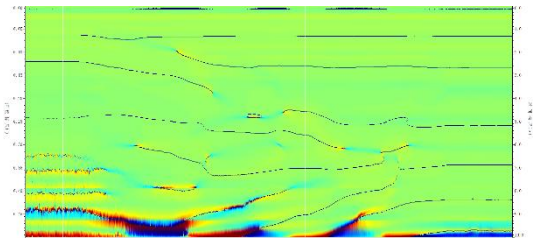

(f) Radargram at a water level of 20cm for 16.5h

Fig. 9 Instantaneous frequency

4.3 Time-domain analysis

Select the initial position of the center point of the GPR for forward detection as the feature point. Fig. 10 shows the single waveform at different time points, while Fig. 11 shows a comparison of the single waveform at the feature points, which clearly shows the reflection pattern at the phreatic lines. From Fig. 11, it can be seen that except for a water level of 20cm for 16.5h, the phreatic lines are relatively low at all other times, and the upper soil layer remains basically dry. The waveform

within 0~2.5ns is basically consistent; At a water level of 20cm and 16.5h, the position of the phreatic lines is higher, and the reflected wave at the phreatic lines is received around 2ns. Therefore, the waveform at the initial stage is significantly different from the rest of the time, and the amplitude at 2ns increases significantly. As the height of the phreatic lines gradually increases, the time for the reflected waves at the phreatic lines to reach the surface of the soil gradually advances, and the amplitude also gradually increases. The reason for this phenomenon is that as the saturation line increases, the propagation distance of electromagnetic waves to the saturation line shortens, energy attenuation decreases, and the amplitude increases on the waveform. The soil below the phreatic lines has a high-water content and dielectric permittivity values, resulting in a large dissipation factor. The electromagnetic wave energy attenuates significantly in the area below the phreatic lines, and the amplitude rapidly decreases [15,16,17].

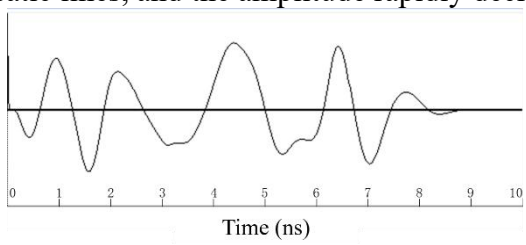

(a)Radargram in dry state

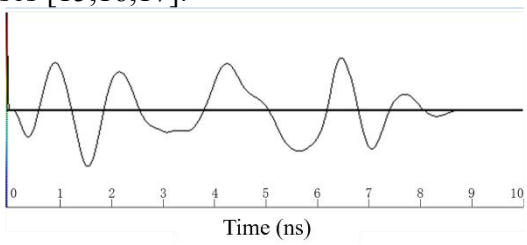

(b)Radargram at a water level of 10cm for 30min

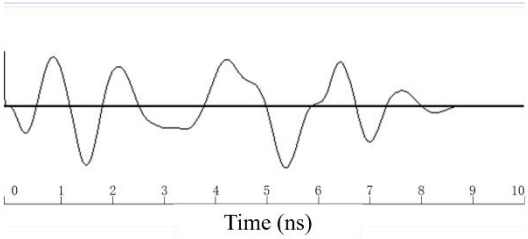

(c) Radargram at a water level of 10cm for 60min

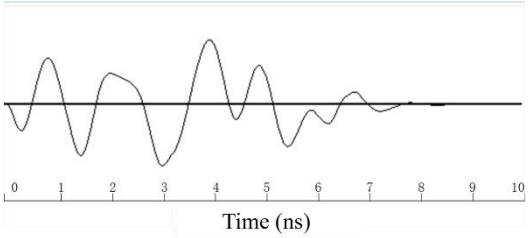

(d) Radargram at a water level of 20cm for 30min

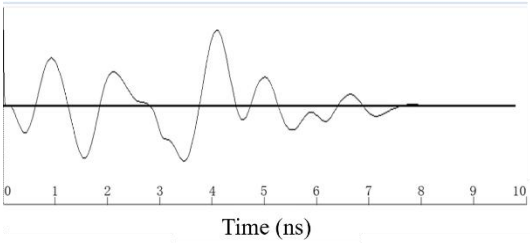

(e) Radargram at a water level of 20cm for 60min

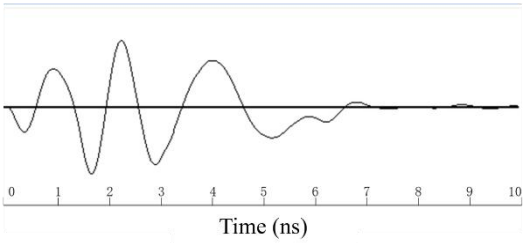

(f) Radargram at a water level of 20cm for 16.5h

Fig.10 Single waveform at feature point

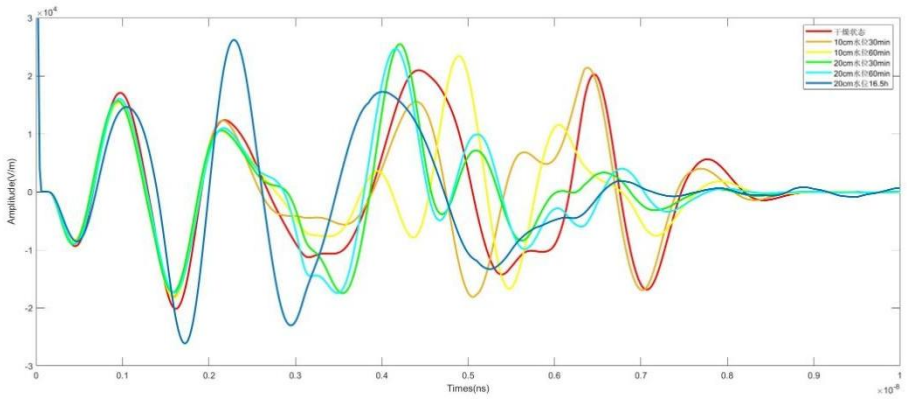

Fig. 11 Comparison of single waveform at feature point

4.4 Frequency-domain analysis

After extracting single channel signals at different time feature points, the frequency spectrum is obtained through Fourier transform, as shown in Fig. 12 and Fig. 13. The frequency distribution ranges from 0 to 1500 MHz, with energy mainly concentrated between 500 and 1000 MHz. The spectrum curve mostly consists of dual main frequencies, with the main frequency around 600MHz and the second main frequency around 900MHz. As the phreatic lines rises, the main frequency gradually shifts towards lower frequencies. This is because as the experiment progresses, the infiltration area of the soil gradually expands, and the overall water content increases. Due to the strong absorption effect of water on electromagnetic waves, high-frequency electromagnetic waves are attenuated.

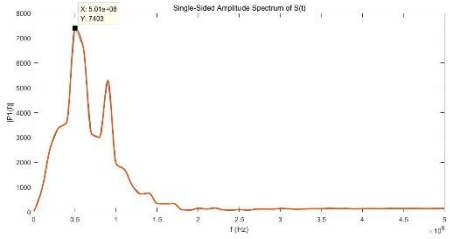

(a)Radargram in dry state

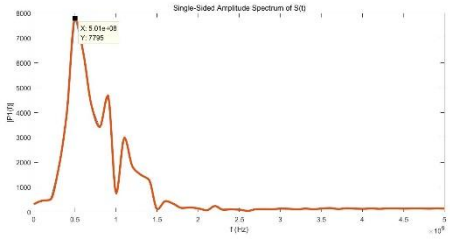

(b)Radargram at a water level of 10cm for 30min

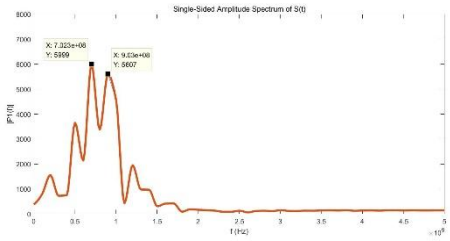

(c) Radargram at a water level of 10cm for 60min

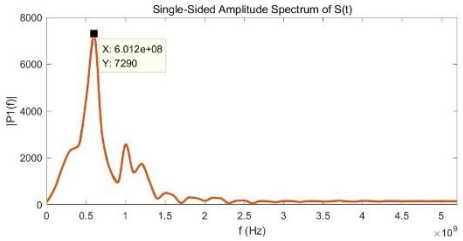

(d) Radargram at a water level of 20cm for 30min

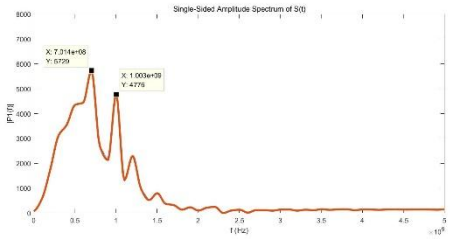

(e) Radargram at a water level of 20cm for 60min

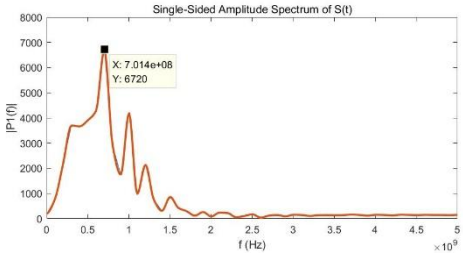

(f) Radargram at a water level of 20cm for 16.5h

Fig. 12 Frequency spectrum at feature point

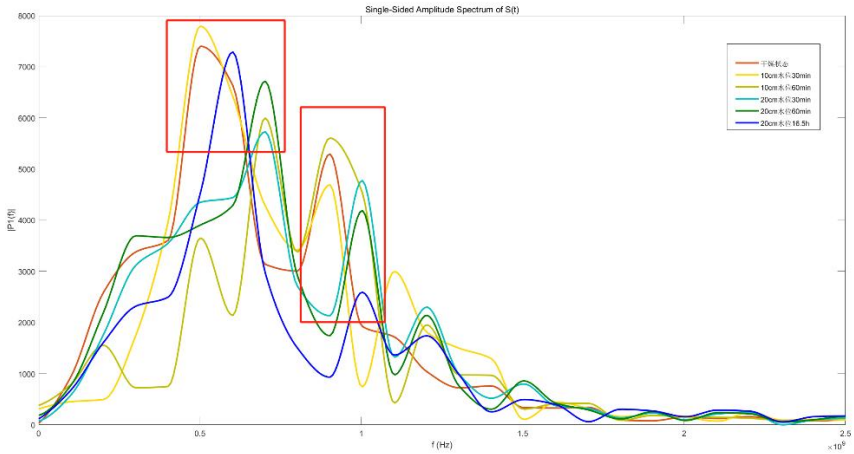

Fig. 13 Comparison of frequency spectrum at feature point

5. Summary

(1) By comparing the radargram and actual observation results, it was found that electromagnetic waves reflected at the phreatic lines, producing obvious reflection signals with some characteristics. Therefore, using GPR to detect the phreatic lines is feasible.

(2) In the radargram, the phreatic lines appear as a tilted strong reflection surface, forming a continuous interface, and its shape is basically consistent with the actual situation of the phreatic lines. In terms of time-domain performance, the amplitude of the reflected wave at the phreatic lines is relatively large, while the amplitude below the phreatic lines rapidly decreases. The depth of the phreatic lines can be easily distinguished in a single waveform; And as the phreatic lines rises, the arrival time of reflected waves gradually advances. In terms of frequency domain performance, the main frequency is around 600MHz, and the second main frequency is around 900MHz. As the saturation line rises, the main frequency gradually shifts towards lower frequencies.

(3) GPR technology, as a non-destructive testing technology, has advantages such as intuitive images and short working cycles. It can quickly and accurately determine the position of the phreatic lines through radar detection results. However, there are also areas that need improvement in this experiment, such as the geotextile blocking between the soil and the water storage area, which has a strong water absorption ability, causing the height of the area infiltrated by the soil to be much higher than the actual water level, and failing to effectively control the height of the phreatic lines by controlling the water level; The storage time at each water level should be appropriately increased to ensure the stability of the phreatic lines before raising the water level. The patterns discovered in the experiment are applicable to the current soil conditions and 900MHz frequency GPR, while the detection patterns under other working conditions or radar frequencies still need further research and verification.

6. Acknowledgements

This research was financially supported by the National Key Research and Development Program of China (2021YFC3090103), Guangdong Province Water Conservancy Technology Innovation Project (2023-02), and the Fundamental Research Funds for Central Public Welfare Research Institutes of China (Y422009、Y422010).

References

[1] Ministry of Water Resources, People's Republic of China. 2020 Statistic Bulletin on China Water Activities. Beijing: China Water&Power Press, 2021.

[2] Li Hongen, Li Zheng, He Yongjun. Typical case study on danger cause of reservoir engineering. Advances in science and technology of water resources, 2014, 34(06): 66-69.

[3] Dong Hang, Liu Sixin, Wang Chunhui, et al. Study on near-surface water content measurement by ground-penetrating radar. Journal of Jilin university (earth science edition), 2009, 39(1): 163-167.

[4] Hong Xiaogang, Zhang Weiguang, Wang Haoyang, Tian Hongbao. Identification technology of structural damages of asphalt pavement based on heterogenous ground-penetrating radar mapping, et al. Journal of Chongqing university (natural science), 2024, 43(04): 7-13.

[5] Zuo Jing, Gao Yuan. Application of Ground Penetrating Radar Technology in Detection of Dams in the Lower Yellow River. Yellow river, 2022, 44(S1): 80-81+87.

[6] Zhou Liming, Zhang Yang. Thickness of glacier and frozen soil in the source region of Changjiang river based on GPR detection. Journal of Changjiang river scientific research institute, 2024, 41(03): 1-8.

[7] İsmail Kaplanvural. Volumetric water content estimation of concrete by particle swarm optimization of GPR data. Construction and building materials, 2023, 375, 130995.

[8] Xu Zeshan, Xiao Min, Chen Jie, et al. Application of ground penetrating radar in detecting the repair effect of road cavity. Geotechnical Investigation & Surveying, 2024(04): 73-78.

[9] Dagenbach A, Buchner JS, Klenk P, et al. Identifying a parameterisation of the soil water retention curve from on-ground GPR measurement. Hydrology and Earth System Sciences, 2013, 17(2): 611-618.

[10] Jafarov EE, Parsekian AD, Schaefer K, et al. Estimating active layer thickness and volumetric water content from ground penetrating radar measurements in Barrow, Alaska. Geoscience Data Journal, 2017, 4(2): 72-79.

[11] Shamir O, Goldshleger N, Basson U, et al. Laboratory measurements of subsurface spatial moisture content by Ground-Penetrating Radar (GPR)Diffraction and Reflection Imaging of Agricultural Soils. Remote Sensing, 2018, 10(10): 1-17.

[12] Leger Emmanuel, Saintenoy Albane, Tucholka Piotr, et al. Hydrodynamic parameters of a sandy soil determined by Ground-Penetrating Radar monitoring of porchet infiltrations. IEEE Journal of Selected Topics in Applied Earth Observations and Remote Sensing, 2016, 9(1): 188-200.

[13] Ran Mi, Deng Shikun, Lu Lixun. Review of Measuring Soil Water Content With Ground- penetrating Radar. Chinese journal of engineering geophysics, 2010, 7(04): 480-486.

[14] Gao Shengguo, Weng Haiteng, Zhu Zhongli. Research progress of ground penetrating radar in monitoring surface soil moisture. Jiangsu Agricultural Sciences, 2017, 45(12): 1-6.

[15] Tan Cai, Pan Zhanzhao, Yuan Mingdao, et al. Application of comprehensive geophysical prospecting technology in emergency detection of dike leakage. Journal of Water Resources & Water Engineering, 2019, 30(5):184-188.

[16] Elena Pettinelli, Giuliano Vannaroni, Barbara Di Pasquo, et al. Correlation between near-surface electromagnetic soil parameters and early-time GPR signals: An experimental study. Geophysics, 2007, 72(2): 25-28.

[17] Fang Hui, Wei Wenbo, Li Yutang. Numerical simulation of the relationship between medium moisture content and ground penetrating radar signals. Geophysical & geochemical exploration, 2009, 33(05): 533-535.